Raman Spectroscopic Studies of Novel Gold-Containing Nanomaterials

By
Lemuel Shui-Lun Tsang

A thesis submitted to the faculty of The University of Mississippi in partial fulfillment of the requirements of the Sally McDonnell Barksdale Honors College.

Oxford

May 2017

Approved by:

_____
Advisor: Professor Nathan Hammer

_____
Reader: Professor Amala Dass

_____
Reader: Professor Jason Ritchie

ABSTRACT

LEMUEL SHUI-LUN TSANG: Raman Spectroscopic Studies of Novel Gold-Containing Nanomaterials

(Under the direction of Dr. Nathan Hammer)

The thiolate-protected gold nanocluster (AuNP) $Au_{38}(SCH_2CH_2Ph)_{24}$ was studied using Raman spectroscopy with particular attention to the vibrational modes of the gold-sulfur interface. Such studies of AuNPs are non-trivial, as these materials are weak scatterers that burn and fluoresce readily. Previous works have successfully studied this class of materials using a rolling circle filter to subtract fluorescence backgrounds, but we set out to develop a method which would suppress fluorescence using more fundamental means. For $Au_{38}(SCH_2CH_2Ph)_{24}$, it was found that data acquisition was most effective using lower-energy excitation wavelengths, which could be predicted based on the UV-Vis absorption spectrum of the cluster. When forced to use higher-energy lasers, significant cooling of samples was required to prevent local heating, i.e. at a temperature of 173 K, a low power of 450 μW using 633 nm excitation was enough to burn a sample of $Au_{38}(SCH_2CH_2Ph)_{24}$. Here, we present the findings of the process by which we developed another method for Raman characterization of AuNPs.

Table of Contents

Copyright Page..... ii

Abstract..... iii

List of Figures..... v

Chapter 1 Introduction..... 1

1.1 Spectroscopy..... 1

1.2 Scattering..... 1

1.3 Raman Spectroscopy..... 2

Chapter 2 Thiolate-Protected Gold Nanoparticles..... 5

2.1 Introduction to Gold Nanoclusters..... 5

2.2 Fluorescence Properties..... 9

2.3 Vibrational Properties..... 10

Chapter 3 Methods..... 13

Chapter 4 Results..... 15

Chapter 5 Conclusions..... 20

List of References..... 21

List of Figures

Figure 1. Gold Particle Size Regimes……. 6

Figure 2. Crystal Structure of $Au_{38}(2\text{-PET})_{24}$…… 13

Figure 3. Comparison of Raman Spectra of Naphthalene……..14

Figure 4. Comparison of Different Phases of Pentafluoroiodobenzene…….. 14

Figure 5. Raman Spectra of Au_{38} Cluster Under 10x Magnification……..15

Figure 6. Comparison of Data Acquisition Under 10x and 100x Magnification…….. 16

Figure 7. Data Acquisition Under 20x Magnification……..17

Figure 8. Raman Spectrum Under 10x Magnification Using 633 nm Excitation…….. 18

Figure 9. Temperature-Controlled Study Under 50x Magnification……..19

Chapter 1 Introduction

1.1 Spectroscopy

Spectroscopy is the study of interactions between electromagnetic radiation and matter. When light collides with a molecule, there are several processes that can occur, e.g. absorption, scattering, impedance, etc. From these events, spectroscopic techniques reveal characteristics of samples such as identity and concentration and describe properties of interest such as rotational, vibrational, and electronic energy level structure. When a molecule is subjected to excitation by light, the energy that it retains is quantified in a system of energy levels, i.e. translational, rotational, vibrational, and electronic. After inducing the excitation of one of these energy levels, the system tends to restore the populations of the energetic states to an equilibrium dictated by the Boltzmann distribution for a certain temperature.

This energetic relaxation occurs through either a nonradiative or a radiative process. For either case, these various processes often produce a detectable change in the light incident on the molecule or the light radiating from the molecule.

1.2 Scattering

There are many different types of scattering including Rayleigh, Mie, Brillouin, and Raman scattering. From a fundamental perspective, each of these represents a change in induced

dipole moment of a molecule, where the induced oscillation of an electric field radiates an electromagnetic field with energy close to that of the incident light.

1.3 Raman Spectroscopy

Here, we present a derivation of Raman scattering from a classical perspective. As stated previously, Raman scattering is a phenomenon that arises from the action of a time-varying electric field on the dipole moment of a molecule, $\vec{\mu}$, through a molecule's polarizability, α. The dipole moment $\vec{\mu}$ is expanded as a Taylor series expansion:

$$\vec{\mu} = \vec{\mu}_0 + \alpha * \vec{E} + \frac{1}{2}\beta * \vec{E}^2 + \cdots \quad (1)$$

Where $\vec{\mu}_0$ is the molecule's permanent dipole moment and higher-order terms represent changes in the dipole moment with respect to the changing electric field, e.g.

$$\alpha = \frac{\partial \vec{\mu}}{\partial \vec{E}} \quad (2)$$

For the expression of Raman scattering, we will assume weak field strengths such that the induced dipole moment $\vec{\mu}_{ind}$ can be approximated using just the first-order terms:

$$\vec{\mu}_{ind} = \alpha * \vec{E} \quad (3)$$

Note that α is a second-rank tensor, while $\vec{\mu}_{ind}$ and $\vec{E}$ are vectors, so Equation (3) would be most accurately expressed as:

$$\begin{bmatrix} \mu_x \\ \mu_y \\ \mu_z \end{bmatrix} = \begin{bmatrix} \alpha_{xx} & \alpha_{xy} & \alpha_{xz} \\ \alpha_{yx} & \alpha_{yy} & \alpha_{yz} \\ \alpha_{zx} & \alpha_{zy} & \alpha_{zz} \end{bmatrix} * \begin{bmatrix} E_{\mathrm{x}} \\ E_{\mathrm{y}} \\ E_{\mathrm{z}} \end{bmatrix} \quad (4)$$

However, we will continue this derivation from scalar values in the interest of simplicity. A given electromagnetic field with a time-dependent electric field of frequency ν is expressed as:

$$E = E_0 \cos(2\pi\nu t) \quad (5)$$

Where E_0 is the initial value of the electric field. Substituting into Equation (5), we obtain a time-dependent expression for the induced dipole moment:

$$\mu_{ind}(t) = \alpha E_0 \cos(2\pi\nu t) \quad (6)$$

The polarizability α of a molecule is dependent on the bond length on which the molecule is vibrating. This requires consideration of $x_e + x(t)$, where which x_e is the equilibrium x position and $x(t)$ is the time-dependent x position due to molecular vibration given by

$$x(t) = x_{max} \cos(2\pi\upsilon_{vib} t) \quad (7)$$

Where x_{max} is the maximum displacement from equilibrium and υ_{vib} is the frequency of vibration of the molecule of interest. This is incorporated into the expression of α as the Taylor series:

$$\alpha\big(x_e + x(t)\big) = \alpha(x_e) + x_{max}\cos(2\pi\upsilon_{vib}t)\frac{d\alpha}{dx} + \cdots \quad (8)$$

Where terms higher-order terms have been neglected for simplicity. Substituting into (8) gives the good approximation:

$$\mu_{ind}(t) = \left[\alpha(x_e) + x_{max}\cos(2\pi\upsilon_{vib}t)\frac{d\alpha}{dx}\right] * E_0 \cos(2\pi\nu t) \quad (9)$$

This can be manipulated into a more intuitive expression for Raman scattering using the trigonometric identity $\cos(x)\cos(y) = \frac{1}{2}[\cos(x-y) + \cos(x+y)]$:

$$\mu_{ind}(t) = \alpha(x_e)E_0\cos(2\pi\nu t) + \frac{d\alpha}{dx}x_{max}E_0\left[\cos\{2\pi(\upsilon + \nu_{vib})t\} + \cos\{2\pi(\upsilon - \nu_{vib})t\}\right] \quad (10)$$

Therefore, when a molecule scatters light, a dipole moment is induced which oscillates and radiates light at the frequencies ν, $(\upsilon + \nu_{vib})$, and $(\upsilon - \nu_{vib})$, which are termed Rayleigh, anti-Stokes, and Stokes scatterings, respectively. Notably, Equation 10 seems to suggest that the intensity of Stokes and anti-Stokes scattering are equal; however, experiment shows that the intensities of each is a function of temperature, with Stokes scattering dominating at 298K. This can be understood by consideration of the relative populations of vibrational energy levels as dictated by the Boltzmann distribution. Note that the intensity of scattering is proportional to $\frac{1}{\lambda^4}$, so assuming a vibrational transition from n=0 to n=1, we find that

$$\frac{I_{anti-Stokes}}{I_{Stokes}} = \frac{(\upsilon + \nu_{vib})^4\, \mathrm{e}^{-\frac{3\mathrm{h}\nu_{vib}}{2k_BT}}}{(\upsilon - \nu_{vib})^4\, \mathrm{e}^{-\frac{\mathrm{h}\nu_{vib}}{2k_BT}}} = \mathrm{e}^{-\frac{\mathrm{h}\nu_{vib}}{k_BT}} \quad (11)$$

Chapter 2 Thiolate Protected Gold

2.1 Introduction to Gold Nanoclusters

The curious properties of gold nanoparticles have been noticed since ancient times, exemplified in their use for the decoration of the Lycurgus Cup from the fourth century A.D.[1] However, a scientific understanding of these materials did not emerge until 1857, when Michael Faraday made the first report of what would later be known as metal nanoparticles with his preparation of a gold colloid by the reduction of a gold salt. He noticed that the ruby-red color of the resulting solution could be made blue depending on the size of the suspended nanoparticles, but he was unable to explain this phenomenon.[2] Shortly after, James Maxwell published a series of works that cumulated into Maxwell's equations, which describe the relations between charge, current, and electric and magnetic fields[3]. In 1908, the absorption and scattering properties of gold were explained when Gustov Mie solved Maxwell's equations for the interaction of light with a single gold nanoparticle, i.e. a sphere with size comparable to the wavelength of incident light.[4] However, it was not until the later development of the band theory of electrons in metals, that the excitation involved in the coloration of colloidal gold was shown to be surface plasmon resonance, i.e. the collective excitation of conduction-band electrons by the resonant interaction between incident light and the frequency of oscillation of electrons[5]. Due to these size dependent properties, gold nanoparticles have been the topic of

heavy research in the past three decades, finding modern applications in a multitude of fields. The topic of this work is a particular class of gold nanoparticles that are protected by a layer of thiolate ligands and are often referred to as nanoclusters. They are characterized by diameters on the scale of one to two nanometers, a direct result of the passivating activity of thiols during the synthesis process[6]. Due to this size regime, thiolate-protected gold nanoparticles (AuNP) exhibit significant quantum confinement effects that heavily influence their electronic and optical properties. This is distinctly different from their larger counterparts, often termed nanocrystals, with diameters from two to one hundred nanometers. These larger particles are those that are found dispersed in the solution of colloidal gold, and as previously mentioned, their electronic structure is characterized by collective excitation through surface plasmon resonance. In contrast, the electronic excitation of AuNPs is discrete, with single electron transitions between the highest-occupied molecular orbital and the lowest-unoccupied molecular orbital.

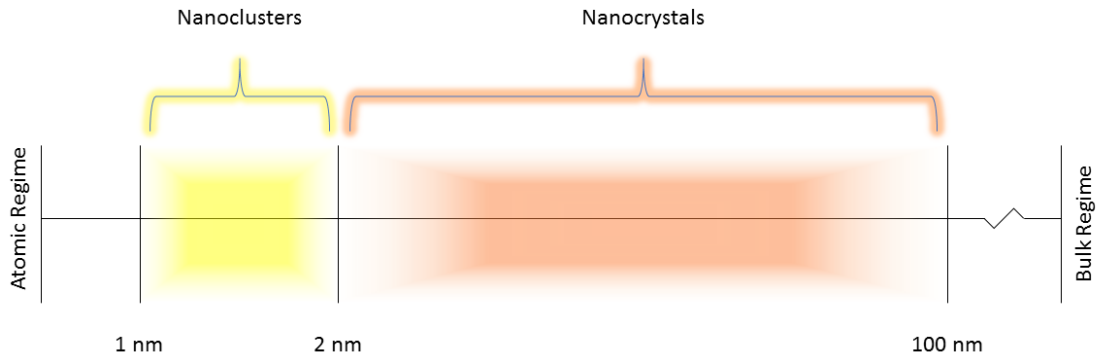

Figure 1: Gold Particle Size Regimes

Here, we present a brief but intuitive extrapolation of the free-electron model for valence electron behavior in bulk metals in order to demonstrate the size regime at which quantum confinement begins to dictate the electronic structure of gold.

Under the free-electron model, we assume no electron-electron or electron-ion interactions, and the Schrodinger equation for one electron is simply

$$\mathcal{H}\Psi = \left(-\frac{\hbar^2}{2m}\nabla^2 + V\right)\Psi = E\Psi \quad (12)$$

Solving by separating *x*, *y*, and *z* variables, i.e.

$$\nabla^2 = \frac{\partial^2}{\partial x^2} + \frac{\partial^2}{\partial y^2} + \frac{\partial^2}{\partial z^2} \quad (13)$$

resulting in

$$\Psi = \Psi_x(x)\Psi_y(y)\Psi_z(z) \quad (14)$$

we find the eigenvalues to be

$$E_n = \frac{\pi^2\hbar^2}{2ma^2}n^2 \quad (15)$$

Where $n^2 = {n_x}^2 + {n_y}^2 + {n_z}^2$ and n_x, n_y, and n_z, are the principal quantum numbers which take on integer values greater than zero, m is the electron mass, and a is the maximum distance of the boundary condition. Notably, each n_x, n_y, and n_z, value generates a circle of radius n, so each n value generates a sphere of radius n which places all states of equal energy onto the same surface area. Therefore, the number of energy states N with energy less than E_n can be modeled as a sphere of volume N. Again, note that n_x, n_y, and n_z are bound by the restrictions previously mentioned, so N is restricted to the positive octant of n-space, which results in

$$N = \frac{1}{8}\left(\frac{4}{3}\pi n^3\right) \quad (16)$$

Substituting with n from Equation (15) gives

$$N = \frac{\pi}{6}\left(\frac{2ma^2}{\pi^2\hbar^2}\right)^{\frac{3}{2}} E^{\frac{3}{2}} \quad (17)$$

To find the density of states, we differentiate Equation (17) with respect to E to find

$$\frac{dN}{dE} = \frac{\pi}{4}\left(\frac{2ma^2}{\pi^2\hbar^2}\right)^{\frac{3}{2}} E^{\frac{1}{2}} = \frac{a^3}{4\pi^2}\left(\frac{2m}{\hbar^2}\right)^{\frac{3}{2}} E^{\frac{1}{2}} \quad (18)$$

The spacing of the electronic energy levels, δ, is then simply the reciprocal of the density of states

$$\delta = \frac{4\pi^2}{a^3}\left(\frac{\hbar^2}{2m}\right)^{\frac{3}{2}} E^{-\frac{1}{2}} \quad (19)$$

Note that a^3 is essentially the volume that bounds the electron, i.e. the volume of the particle. As the number of atoms decreases, a^3 also decreases, which leads to an increase in δ. We illustrate this using the thermal energy at 298 K to bridge the size-dependent δ gap

$$\delta = k_B T \quad (20)$$

We solve Equation (19) using the highest occupied energy level of gold, $E = 8.8 * 10^{-27}$ J to find that a^3 is approximately $5 * 10^{-27}$m^3, which gives a particle diameter of approximately 1.7 nm. Indeed, it is at about this size that surface plasmon resonance is no longer supported by gold particles, and the molecular, HOMO to LUMO single-electron excitation is made manifest. A recent work studying a series of size-differentiated AuNPs using femtosecond transient absorption spectroscopy confirmed this, finding three regimes of gold nanoparticles based on the sensitivity to laser power of electron-phonon coupling time. The metallic regime included particles larger than 2.3 nm, i.e. $Au_{>333}$; the transition regime included particles between 2.3 and 1.7 nm, i.e. Au_{333} to Au_{144}; and the molecular regime included particles smaller than 1.7 nm, i.e. $Au_{<144}$[7].

Such methodology is a testament to the progress that has been made in the synthesis of AuNPs since the first report of its synthesis in 1994[6]. In previous years, physical and chemical characterization of AuNPs was severely hindered by limitations in synthetic technique that resulted in polydisperse samples. Recent advances have allowed for the synthesis of atomically precise $Au_n(SR)_m$ samples; this, in turn, paved the way for the x-ray crystallographic determination of structure for $Au_{25}(SR)_{18}$[8], $Au_{38}(SR)_{24}$[9], and $Au_{102}(SR)_{44}$[10]. These breakthroughs allowed for a basis from which the stability of these molecules could be understood, i.e. the electronic and geometric contributions made by the gold-sulfur bonds. It is now well established that the clusters consist of a metal core and a passivating thiolate ligand layer, where the ligands consist of a gold atom sandwiched between two sulfur atoms in the form SR(-Au-SR); in addition, the Au atoms can be conceptually separated by basis of chemical states. The Au atoms present in the metal core are electrically neutral while those in the ligands are positively charged due to oxidation by the sulfur atoms[11].

These gold-sulfur bonds are significant for several reasons. As previously mentioned, they underlie the formation of these ultra-small gold nanoclusters, so they have a stabilizing effect that is particularly evident for certain “magic numbers” of gold atoms and ligands. There is ongoing work in the development of models for the explanation of this stabilizing effect, e.g. the superatom complex[12] and grand unified[13] models, but much remains to be done.

2.2 Fluorescence Properties

In recent years, significant efforts have been made for the development of AuNPs as sensors and imagers due to their fluorescent properties. Particular attention has been paid to the biomedical applications, where the biocompatibility of these compounds make them good

fluorophores for a variety of applications[14]. For example, they have been developed into sensors for Hg^{2+} in living HeLa cells[15] and for the protein Cystatin C[16]; they have also seen application as imagers, e.g. upon biosynthesis by cancer cells[17]. The fluorescence of AuNPs is believed to originate from the combination of free-electron transitions of the Au core and ligand-to-metal charge transfer (LMCT) through the Au-S interface[18,19].

Regarding the cluster-size dependence of fluorescence, the previously shown derivation indicates that the size of the particle is critical to its fluorescence. Further note that for the condition

$$\delta = k_B T = \frac{4\pi^2}{a^3}\left(\frac{\hbar^2}{2m}\right)^{\frac{3}{2}} E^{-\frac{1}{2}} \quad (21)$$

Where T is low, there is insufficient thermal energy to breach the δ gap, which is macroscopically manifested in a lower number of fluorescing particles, i.e. decreased fluorescence intensity[19].

Regarding the LMCT dependence of fluorescence, AuNP fluorescence has been shown to be enhanced in both quantum yield and fluorescence intensity by increasing electron-donating capabilities of the thiolate ligands[18].

2.3 Vibrational Properties

Vibrational spectroscopy is a sensitive method of interrogating molecular structure, and considering the importance of structure in the stability and electronic properties of AuNP, it should come as no surprise that significant effort has been put into this area. FTIR studies have shown that the mid-IR range relates almost purely to the ligands[20], and this is also evident in

vibrational circular dichroism studies of ligand chirality transfer[21]. Early far-IR and computational studies established the vibrational modes of the Au-S interface as occupying the 200 to 350 cm^{-1} range[22,23]; this was in agreement with high resolution electron energy loss spectroscopic studies of a closely related, better established class of compounds, the thiolated, self-assembled monolayers of gold[24]. Notably, the Au−Au core modes predicted in the <200 cm^{-1} region should be very weak in the far-IR spectrum but strong in the Raman spectrum due to low polarity but high polarizability[23]. With this knowledge, previous works have conducted Raman spectroscopic studies of AuNPs with apparent success[25,26], but a more recent work highlighted several difficulties in the Raman characterization of this class of compounds that were seemingly ignored in previous studies. Specifically, AuNPs are weak scatterers that absorb strongly in the visible region. This results in local heating, which causes thermal decomposition of the sample; further, the samples fluoresce heavily upon absorption of light, producing a very large background signal[27]. Nevertheless, systematic far-IR and Raman spectroscopic studies on Au clusters of various sizes protected by the ligand 2-phenylethanethiolate (2-PET) have assigned, with the help of DFT calculations, various Au-S vibrational modes, namely the Au-S-C bending modes at 180 cm^{-1}, the radial Au-S stretching modes at 220-280 cm^{-1}, and the tangential Au-S stretching modes at 320 wavenumbers[27,28]. A more recent study of a series of Au_{25} clusters with varying thiolate ligand alkane lengths, i.e. $Au_{25}(SC_nH_{2n+1})_{18}$ with n = 2, 3, 4, 5, 6, 8, 10, 12, and 14, found a strong but unsystematic dependence of the Au-S spectral features on alkyl chain length due to coupling of the modes with other vibrations of the entire chain[29]. Notably, there were several limitations to the Raman studies discussed above. As previously mentioned, the extraction of Raman spectra from AuNPs is non-trivial because of local heating and fluorescence. The most recent studies published have prevented thermal composition by rotating the sample at about 3000 rpm. A laser power between 5-8 mW was used, resulting in a large,

unreproducible background dominated by fluorescence, so a rolling circle filter was applied to subtract the broadband background[30]. However, this required a cutoff parameter at ~160 cm^{-1}, so the previously mentioned low-energy Au-Au vibrations of the Au core could not be probed.

To this end, we set out to develop a method to view these phonon modes, as we have sensitive instrumentation capable of viewing vibrational modes as low as 5 cm^{-1}. In addition, we wanted to prepare the groundwork for future studies of AuNPs with varying types of ligands, e.g. bulky, aromatic, etc.

Chapter 3 Methods

$Au_{38}(2\text{-PET})_{24}$ nanoclusters were synthesized by Milan Rambukwella from the Dass Group. Samples were dissolved in dichloromethane and deposited on glass slides using pipette bulbs. Raman spectra were collected using a Horiba LabRAM HR Evolution Raman Spectrometer with 633 and 785 nm lasers with laser power varying from 1.4 to 500µW. These wavelengths were chosen to minimize absorption of light, as determined by UV-Vis spectroscopy[31].

Temperature controlled studies were carried out using a Linkam Scientific THMS600 Temperature Controlled Stage for temperature ranges from 123 to 298K. Note that temperature controlled Raman is a powerful tool, allowing for phase change studies or simply better resolution via eliminating noisy rotational energy level excitations.

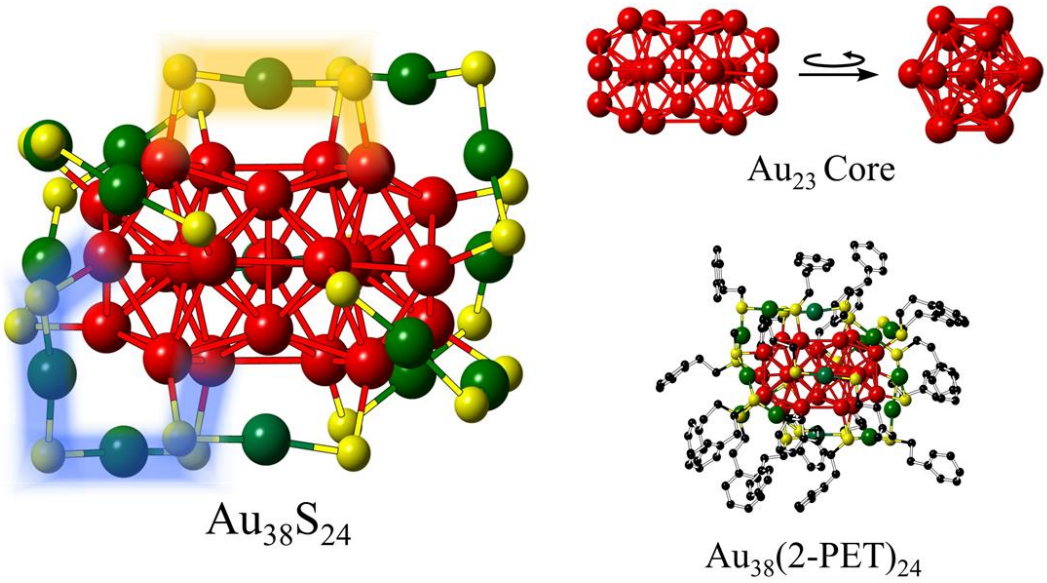

Figure 2: Crystal Structure of $Au_{38}(2\text{-PET})_{24}$; shown are the 23 atom Au core, the Au-S interface, and the full molecule; highlighted are the monomeric S-Au-S ligands in orange and the dimeric S-Au-S-Au-S ligands in blue.

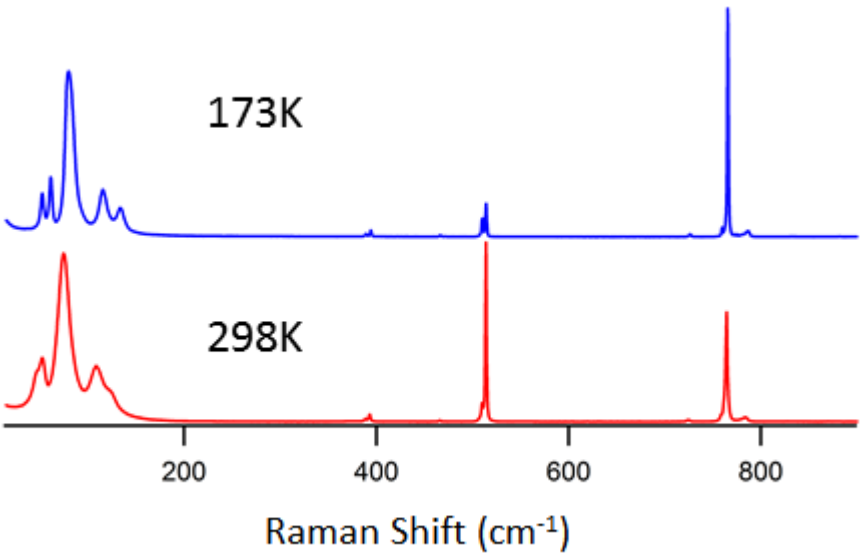

Figure 3: Comparison of Raman Spectra of Naphthalene; at 173K, the modes around 100 cm^{-1} are resolved

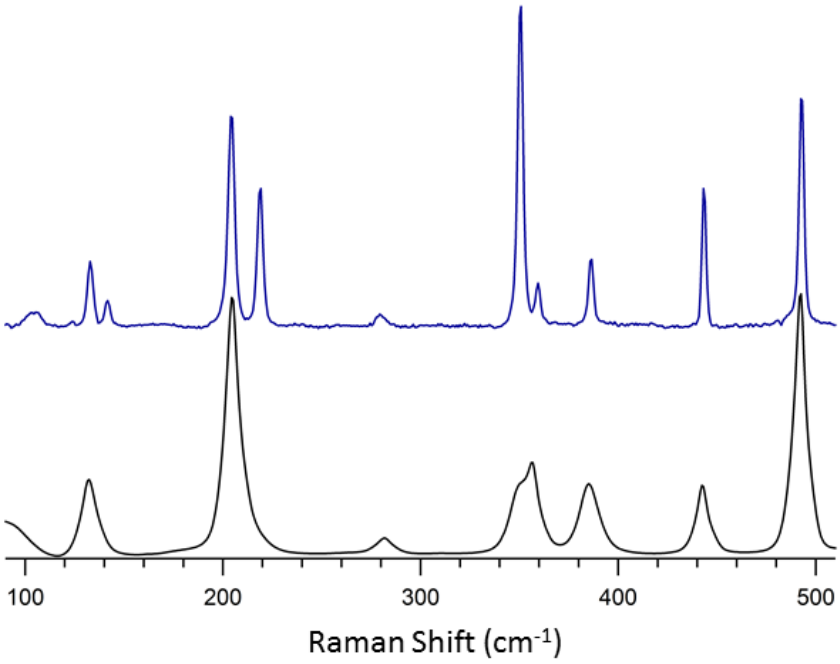

Figure 4: Comparison of Different Phases of Pentafluoroiodobenzene; at ~213K (blue), the liquid solidifies, further elucidating its vibrational structure

Chapter 4 Results

Early on, we could obtain reproducible Raman data under a 10x objective microscope focus lens using the 785 nm laser. It was found that high concentration of sample deposited on a glass slide yielded large, featureless black spots on which Raman spectra could be collected. However, the spectral features in the 250 to 350 cm^{-1} range were unclear, and the proper focus was difficult to find due to the lack of topographical features under the microscope.

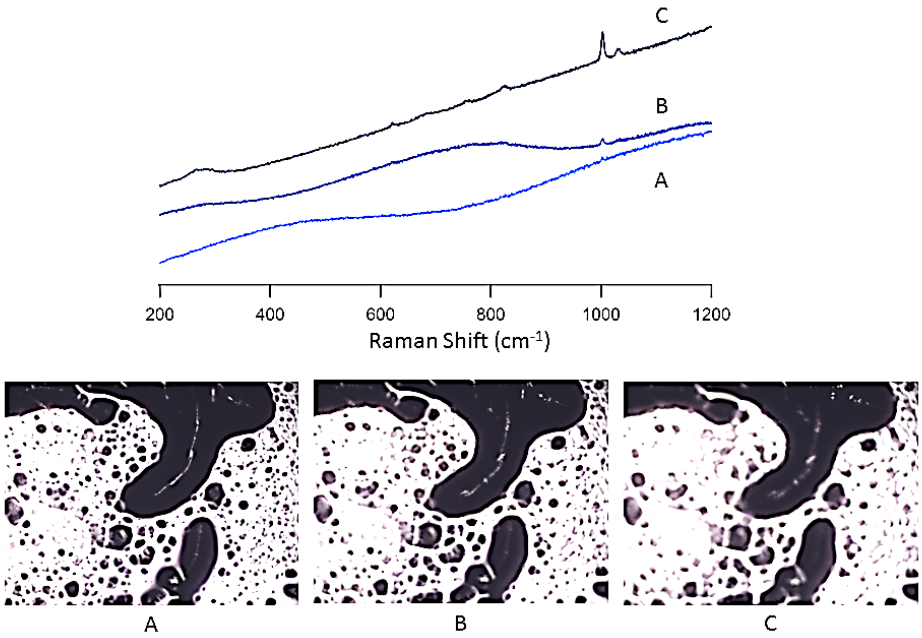

Figure 5: Raman Spectra of Au_{38} Cluster Under 10x Magnification; the large background is from the previously mentioned fluorescence of the AuNP; it is evident that the correct focus cannot be determined based on the visual clarity of local topography.

To resolve these issues, we used higher magnifications, which would firstly yield higher resolution due to smaller focus areas for the uptake of signal light and secondly allow for easy focusing due to increased visual clarity in the area of focus. However, it was found that data

acquisition became significantly more difficult upon use of higher magnifications, shown in Figure 6. After extensive testing with the 50x long-working-distance and 100x objective lenses, several conclusions were made. First, the focus had to be out of focus; second, the Raman signal was extremely sensitive to this focus, particularly at higher magnifications. The former can be rationalized by considering that the wavelength of the laser is slightly longer than that of visible light.

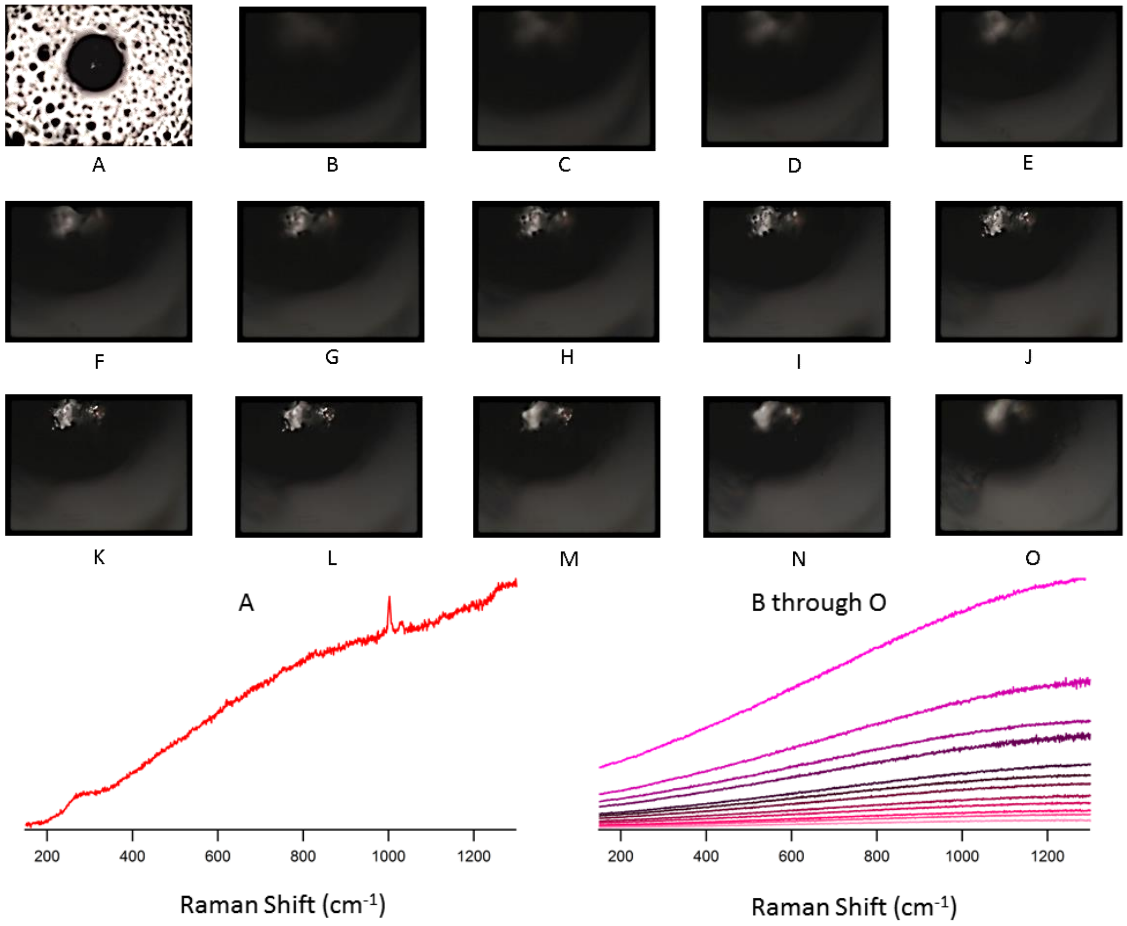

Figure 6: Comparison of Data Acquisition Under 10x and 100x Magnification; successful data acquisition using 10x magnification was followed by unsuccessful attempts using 100x magnification at a series of foci.

We then incrementally increased the magnification, finding success with the 20x objective lens. We noticed an abnormally high sensitivity to focus, as shown in Figure 7. The Raman signal varies strongly in the series A to C, despite the change in focus being barely

detectable. In addition, this constituted the first observation for our group of the more refined vibrational modes of the gold sulfur bonds, confirming our approach for increasing magnification and further establishing the need for very specific focus.

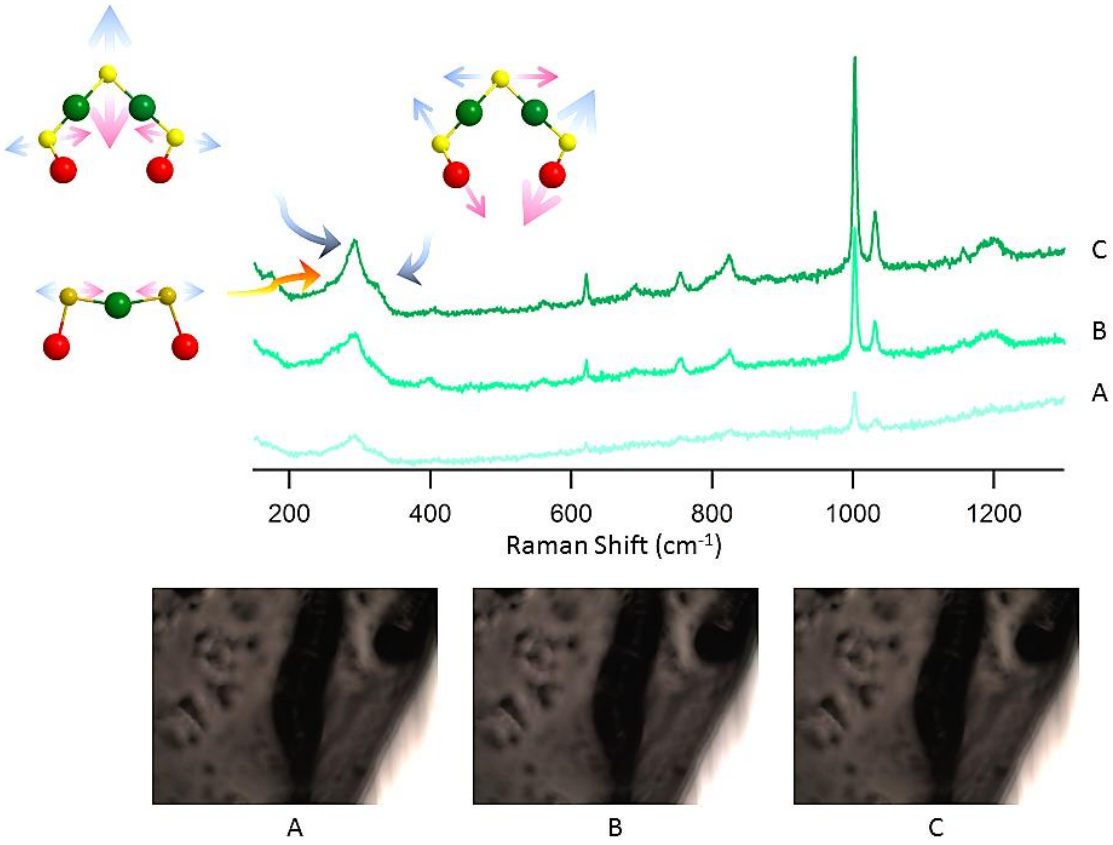

Figure 7: Data Acquisition Under 20x Magnification; the series A through C show that Raman signal is extremely sensitive to focus; the Au-S vibrational modes in spectrum C are assigned with reference to previous works[23,27,29].

From here, we proceeded to data acquisition using the 633 nm laser, which we hoped would circumvent the magnification difficulties of the 785 nm laser due to being the same wavelength as the light observed by the focusing microscope. However, this laser line was both of a higher energy and absorbed more heavily by the Au_{38} cluster, so to prevent thermal decomposition by local heating, we used low laser powers for excitation and conducted Raman studies in a temperature controlled stage. As mentioned earlier, it is predicted that fluorescence will increase at lower temperatures, but this was not significantly observed.

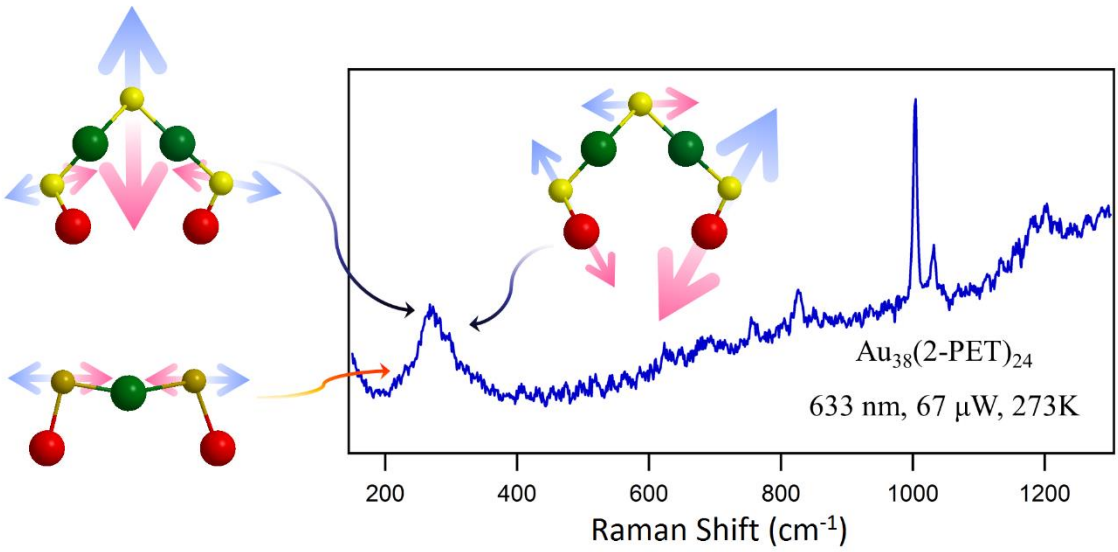

Figure 8: Raman Spectrum Under 10x Magnification Using 633 nm Excitation

Figure 8 shows an early success under 10x magnification: the Raman signal could resolve some of the Au-S modes. We then hoped that we would be able to resolve more spectral details by increasing the magnification, i.e. using the same method applied to the 785 nm laser. Notably, the increase in power density needed to be accounted for by decreasing laser power, and the focus of the microscope was the same as the focus of the laser.

Shown in Figure 9 are the results of these studies, which found that with increasing laser power, the Raman signal evidently increased. However, a power of 140 μW was insufficient to resolve the desired Au-S details, and further increasing the power resulted in thermal decomposition of the sample, despite a sample temperature of 173K.

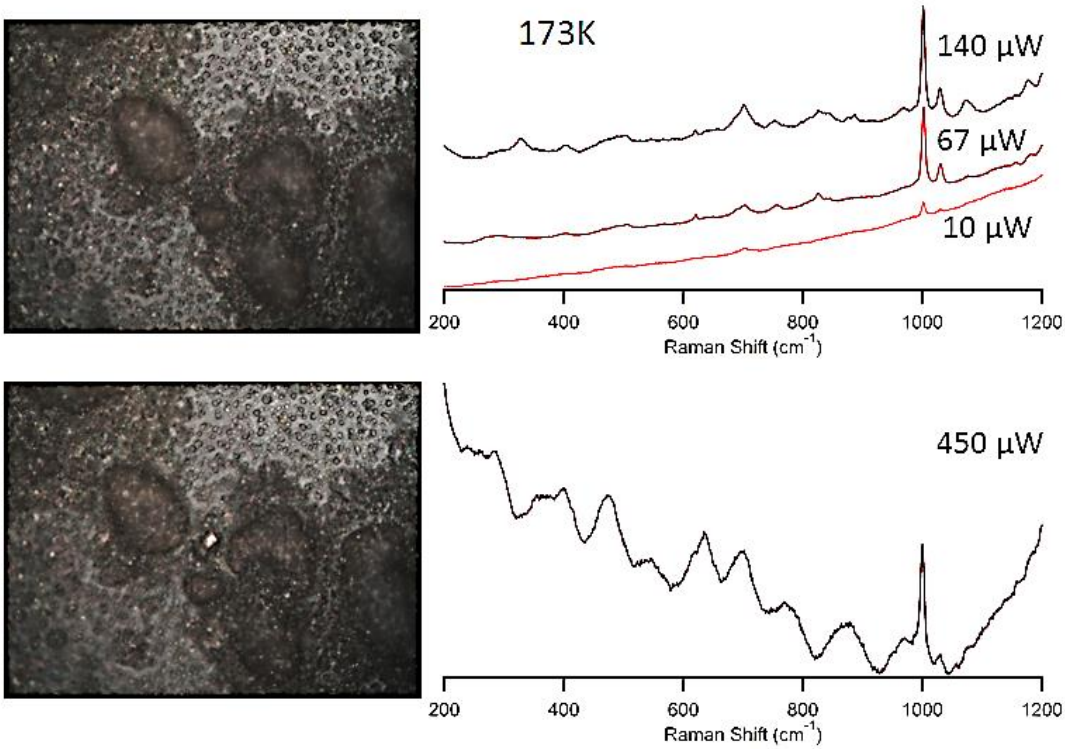

Figure 9: Temperature-Controlled Study Under 50x Magnification Using 633 nm Excitation; Raman spectra acquired at 173K using 10 µW, 67 µW, 140 µW, and 450 µW laser power; there is clear evolution of Raman signal, but the Au-S vibrations are not well resolved up till 140 µW.

Chapter 5 Conclusions

Here, we used Raman spectroscopy to characterize the gold nanocluster $Au_{38}(2\text{-PET})_{24}$ with limited success. The objectives were to develop a method for studying this class of materials, which burn easily and fluoresce readily, and to view the low-energy phonon modes of the Au core, which have yet to be studied by others due to technical limitations of the rolling circle filter for fluorescence subtraction. To this end, we utilized low-power, low-energy excitation wavelengths and temperature-control to successfully extract Raman signals from samples. The resolution of data shows spectral resolution equal to that of previous works, but the low-energy vibrational modes remain unresolved. Future work should attempt studies using the 633 nm laser at lower temperatures, higher powers, and high magnifications, as the trends seen in this work indicate that the Au-S vibrations could be resolved with greater clarity. Alternatively, a method for even deposition of sample on slides could be used to both facilitate data acquisition and to increase spectral resolution at lower magnifications. From here, one could begin studies on the influence of different types of ligands on the Au-S interface.

List of References

1. Freestone, I., Meeks, N., Sax, M. & Higgitt, C. The Lycurgus Cup --- A Roman nanotechnology. *Gold Bull.* **40,** 270–277 (2007).

2. Faraday, M. The Bakerian Lecture: Experimental Relations of Gold (and Other Metals) to Light. *Phil. Trans. R. Soc. Lond.* **147,** 145–181 (1857).

3. Maxwell, J. C. A Dynamical Theory of the Electromagnetic Field. *Philos. Trans. R. Soc. London* **155,** 459–512 (1865).

4. Mie, G. Beiträge zur Optik trüber Medien, speziell kolloidaler Metallösungen. *Ann. Phys.* **330,** 377–445 (1908).

5. Ghosh, S. K. & Pal, T. Interparticle coupling effect on the surface plasmon resonance of gold nanoparticles: From theory to applications. *Chem. Rev.* **107,** 4797–4862 (2007).

6. Brust, M., Walker, M., Bethell, D., Schiffrin, D. J. & Whyman, R. Synthesis of thiol-derivatised gold nanoparticles in a two-phase Liquid-Liquid system. *J. Chem. Soc.{,} Chem. Commun.* 801–802 (1994). doi:10.1039/C39940000801

7. Zhou, M. *et al.* Evolution from the plasmon to exciton state in ligand-protected atomically precise gold nanoparticles. *Nat. Commun.* **7,** 13240 (2016).

8. Heaven, M. W., Dass, A., White, P. S., Holt, K. M. & Murray, R. W. Crystal Structure of the Gold Nanoparticle [N(C8H17)4][Au25(SCH2CH2Ph)18]. *J. Am. Chem. Soc.* **130,** 3754–3755 (2008).

9. Qian, H., Eckenhoff, W. T., Zhu, Y., Pintauer, T. & Jin, R. Total Structure Determination of Thiolate-Protected Au38 Nanoparticles. *J. Am. Chem. Soc.* **132,** 8280–8281 (2010).

10. Jadzinsky, P. D., Calero, G., Ackerson, C. J., Bushnell, D. A. & Kornberg, R. D. Structure of a Thiol Monolayer-Protected Gold Nanoparticle at 1.1 Å Resolution. *Science (80-.).* **318,** 430 LP-433 (2007).

11. Häkkinen, H., Walter, M. & Grönbeck, H. Divide and Protect: Capping Gold Nanoclusters with Molecular Gold−Thiolate Rings. *J. Phys. Chem. B* **110,** 9927–9931 (2006).

12. Walter, M. *et al.* A unified view of ligand-protected gold clusters as superatom complexes. *Proc. Natl. Acad. Sci.* **105,** 9157–9162 (2008).

13. Xu, W. W., Zhu, B., Zeng, X. C. & Gao, Y. A grand unified model for liganded gold clusters. *Nat. Commun.* **7,** 13574 (2016).

14. Luo, Z., Zheng, K. & Xie, J. Engineering ultrasmall water-soluble gold and silver nanoclusters for biomedical applications. *Chem. Commun.* **50,** 5143–5155 (2014).

15. Shang, L. *et al.* Microwave-assisted rapid synthesis of luminescent gold nanoclusters for sensing Hg2+ in living cells using fluorescence imaging. *Nanoscale* **4,** 4155–4160 (2012).

16. Lin, H. *et al.* Immune-independent and label-free fluorescent assay for Cystatin C detection based on protein-stabilized Au nanoclusters. *Biosens. Bioelectron.* **41,** 256–261 (2013).

17. Wang, J. *et al.* In vivo self-bio-imaging of tumors through in situ biosynthesized fluorescent gold nanoclusters. *Sci. Rep.* **3,** 1157 (2013).

18. Wu, Z. & Jin, R. On the Ligand's Role in the Fluorescence of Gold Nanoclusters. *Nano Lett.* **10,** 2568–2573 (2010).

19. Chen, L.-Y., Wang, C.-W., Yuan, Z. & Chang, H.-T. Fluorescent Gold Nanoclusters: Recent

Advances in Sensing and Imaging. *Anal. Chem.* **87,** 216–229 (2015).

20. Farrag, M., Tschurl, M., Dass, A. & Heiz, U. Infra-red spectroscopy of size selected Au25, Au38 and Au144 ligand protected gold clusters. *Phys. Chem. Chem. Phys.* **15,** 12539–12542 (2013).

21. Dolamic, I., Varnholt, B. & Bürgi, T. Chirality transfer from gold nanocluster to adsorbate evidenced by vibrational circular dichroism. *Nat. Commun.* **6,** 7117 (2015).

22. Petroski, J., Chou, M. & Creutz, C. The coordination chemistry of gold surfaces: Formation and far-infrared spectra of alkanethiolate-capped gold nanoparticles. *J. Organomet. Chem.* **694,** 1138–1143 (2009).

23. Tlahuice-Flores, A., Whetten, R. L. & Jose-Yacaman, M. Vibrational Normal Modes of Small Thiolate-Protected Gold Clusters. *J. Phys. Chem. C* **117,** 12191–12198 (2013).

24. Kato, H. S., Noh, J., Hara, M. & Kawai, M. An HREELS Study of Alkanethiol Self-Assembled Monolayers on Au(111). *J. Phys. Chem. B* **106,** 9655–9658 (2002).

25. Parker, J. F., Choi, J.-P., Wang, W. & Murray, R. W. Electron Self-exchange Dynamics of the Nanoparticle Couple [Au25(SC2Ph)18]0/1− By Nuclear Magnetic Resonance Line-Broadening. *J. Phys. Chem. C* **112,** 13976–13981 (2008).

26. Price, R. C. & Whetten, R. L. Raman Spectroscopy of Benzenethiolates on Nanometer-Scale Gold Clusters. *J. Phys. Chem. B* **110,** 22166–22171 (2006).

27. Varnholt, B. *et al.* Structural Information on the Au–S Interface of Thiolate-Protected Gold Clusters: A Raman Spectroscopy Study. *J. Phys. Chem. C* **118,** 9604–9611 (2014).

28. Dolamic, I., Varnholt, B. & Burgi, T. Far-infrared spectra of well-defined thiolate-

protected gold clusters. *Phys. Chem. Chem. Phys.* **15,** 19561–19565 (2013).

29. Varnholt, B. *et al.* Vibrational Coupling Modulation in n-Alkanethiolate Protected Au25(SR)180 Clusters. *J. Phys. Chem. C* **120,** 25378–25386 (2016).

30. Brandt, N. N., Brovko, O. O., Chikishev, A. Y. & Paraschuk, O. D. Optimization of the Rolling-Circle Filter for Raman Background Subtraction. *Appl. Spectrosc.* **60,** 288–293 (2006).

31. Dolamic, I., Knoppe, S., Dass, A. & Bürgi, T. First enantioseparation and circular dichroism spectra of Au(38) clusters protected by achiral ligands. *Nat. Commun.* **3,** 798 (2012).